Desalination and Water Treatment
www.deswater.com

doi: 10.5004/dwt.2017.21672

98 (2017) 326–335
December

Effect of morphology on adsorption kinetics of magnesium oxide for the removal of methyl orange

Yong Liu[a], Ming Huang[a], Yaohui You[a], Donghai Zhu[b], Xiaojing Fu[a], Jinhai Yuan[c], Xiaogang Zheng[a,*], Jing Wen[b,*]

[a]*College of Chemistry and Chemical Engineering, Neijiang Normal University, Neijiang Sichuan 641100, China, email: bassly@163.com (Y. Liu), 1043406073@qq.com (M. Huang), allenyouyaohui@163.com (Y. You), fu-xj2007@163.com (X. Fu), Tel./Fax 086-832-2341577, 086-971-7762180, email: zhengxg123456@163.com (X. Zheng)*
[b]*Key Laboratory of Comprehensive and Highly Efficient Utilization of Salt Lake Resources, Qinghai Institute of Salt Lakes, Chinese Academy of Sciences, Xining, 810008, China, email: zhudonghai-2001@163.com (D. Zhu), Tel./Fax 086-832-2341577, 086-971-7762180, email: wj580420@163.com (J. Wen)*
[c]*College of Chemistry and Chemical Engineering, Chongqing University of Science & Technology, Chongqing 401331, China, email: wenzhuyuan@126.com (J. Yuan)*

Received 2 May 2017; Accepted 17 November 2017

ABSTRACT

MgO nanomaterials with different microstructure morphologies such as nanorods (MgO_R), flower-like (MgO_F), and lamellar (MgO_L) were prepared for the adsorption performance in the removal of methyl orange. MgO_R sample exhibited better adsorption ability in comparison to MgO_F and MgO_L sample due to its higher specific surface area, larger pore volume,and more available active sites. Langmuir isotherm model described well with the adsorption isotherm of MgO samples for the removal of methyl orange, and the pseudo-second-order adsorption model fitted well with the adsorption process of dye removal. The intra-particle diffusion model demonstrated that the adsorption process of different MgO samples was the combination of immediate surface diffusion and slow pore diffusion, in which the rate-determining step was the boundary layer diffusion.

Keywords: MgO nanomaterials; Micro-structure morphology; Methyl orange; Adsorption isotherms; Adsorption kinetics

1. Introduction

As one of promising adsorbents, magnesium oxide (MgO) nanomaterial has been widely paid attention because of its environment-friendly nature, excellent adsorption capacity, and low regeneration cost [1]. MgO has been reported for the efficient removal of organic pollutants [2,3] and heavy metal ions in industrial wastewater [4–8] and capture CO_2 from exhaust gas [9–12]. In recent years, the multi functional MgO-based composites have been explored to meet the need of high adsorption capacity, easy separation, and self-regeneration [13–16]. MgO nanoparticles immobilized by chitosan [13] and mesoporous carbon [14] are suitable for the enhanced removal efficiency of orange dyes and CO_2 capture. The combination between metal ions and active sites of MgO also exhibits remarkable antibacterial efficiency [16].

It's widely accepted that the adsorption capacity of MgO adsorbent is greatly affected by its microstructure and surface basicity. These physico chemical properties of MgO-based materials are intensively determined by the synthesis routes and the processing conditions. MgO nanomaterials are mainly synthesized by the thermal decomposition of magnesium carbonate or hydroxide, hydrothermal route, sol-gel process, sono chemical reaction, and spray pyrolysis [17–22]. The optimal parameters of synthesis approach is likely to achieve a regular micro-

*Corresponding author.

structure as well as uniform size of MgO nanomaterials. Numerous works focused on the effects of particle size and pore structure on MgO-based adsorbent, especially mesoporous MgO promoted with alkali salt ($NaNO_3$, KNO_3, or Na_2CO_3) for excellent sorption capacity of CO_2 capture [23,24]. Nevertheless, less attention focused on the influence of nano-MgO morphology on the adsorption capacity.

The adsorption kinetics is a critical issue for understanding the adsorption rate and adsorption capacity of MgO adsorbent in industrial application. Previous papers have been widely investigated the adsorption kinetics of MgO-based adsorbents for the CO_2 capture [25–28], removal of organic dyes [29–34] and heavy metal ions [35–37]. Song et al. [25] proposed that pseudo-second order model accurately predicted the CO_2 adsorption behaviors of porous MgO under a wide range of CO_2 partial pressure and adsorption temperature, where porous MgO showed a rapid initial CO_2 uptake and a subsequent slow adsorption process. Mahmoud et al. [32] suggested that pseudo-first order model fitted well with the experimental values of adsorption capacity of nano-MgO for removal of Remazol Red RB-133 dye. Xiong et al. [7] reported that the adsorption of Cd(II) and Pb(II) on nano-MgO were pseudo-second order model and Langmuir model, respectively. Different morphology of MgO nanoparticles exhibited different adsorption behavior for the dyes and heavy metals [38–43]. These works provided a better explanation of the adsorption mechanism and a potential prediction of adsorption behavior of nano-MgO. No details about the effect of morphology of nano-MgO on the adsorption kinetics and the rate-limiting step in the removal of methyl orange has been reported.

In this paper, MgO nanomaterials with different nanostructures (lamellar, flower-like, and nanorods) were employed to investigate the adsorption kinetics of removal of methyl orange dye. The adsorption isotherms, adsorption kinetic models, and intra-particle diffusion model were also carried out for the evaluation of adsorption isotherm and mechanism of obtained MgO samples with different nanostructures.

2. Experimental

2.1. Preparation of MgO

Flower-like MgO (MgO_F) and lamellar MgO (MgO_L) nanomaterials were prepared by a paraffin-in-water micro-emulsion system in previous work [38]. Fig. 1 presents the schematic flow chart for the synthesis of MgO_F and MgO_L nanoparticles. Typically, 4 g paraffin, 1 g polyethylene glycol (MW = 10,000), and 1 gcetyltri methyl ammonium bromide were added into a high-shear mulser with 200 mL ethanol solution (50 wt%) and emulsified at 343 K for 20 min. 50 mL $MgCl_2{\cdot}6H_2O$ solution (2.0 mol L^{-1}) and 50 mL Na_2CO_3 solution (2.0 mol L^{-1}) were concurrently injected into above paraffin emulsion and intensely stirred at 343 K for 1 h. The generated Mg-based suspension was filtered, washed with deionized water three times, dried at 323 K for 10 h, and calcined at 923 K for 6 h to obtain MgO_F sample. According to the above synthesis process, MgO_L sample was generated through the heating treatment at 1123 K for 6 h.

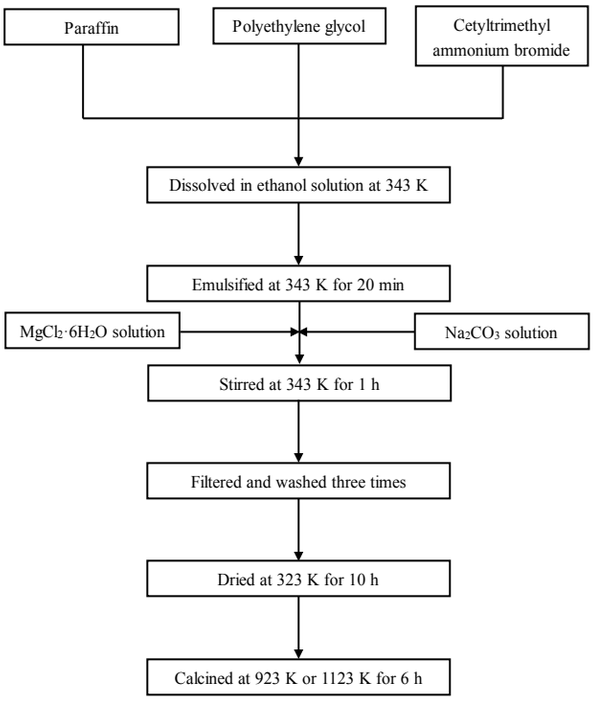

Fig. 1. Schematic flow chart for the preparation steps of MgO and MgO nanoparticles.

MgO nanorods (MgO_R) were synthesized via calcining magnesium oxy sulfate whiskers (5 $Mg(OH)_2{\cdot}MgSO_4{\cdot}3H_2O$) prepared by hydrothermal method [44,45]. In a typical process, 14.80 g $MgSO_4{\cdot}7H_2O$ and 2.00 g NaOH were added into 60 mL deionized water and stirred at room temperature for 2 h. The above slurry solution was transferred to a 100 mL Teflon-lined stainless steel autoclave and treated at 473 K for 6 h. After gradually cooled down to room temperature, the synthesized product was filtrated, washed with deionized water three times, dried at 353 K for 10 h, and calcined at 1173 K for 6 h to obtain MgO_R sample.

2.2. Characterization of MgO

The crystalline phases of as-synthesized MgO samples were detected via Bruker D8 Advance X-ray Powder Diffractometer with a spectra range of 20~80° and a scan step rate of 2° min^{-1}. Field emission scanning electron microscopy (FESEM, Hitachi S-4800) and transmission electron microcopy (TEM, G220) were employed to obtain the nanostructure and particle size of MgO samples. The textural properties of MgO samples were observed by N_2 adsorption-desorption method on a NOVA-2020 material physical structure determinate. Fourier transforms infrared spectra (FT-IR) were obtained on a Bruker VECTORTM 22 FTIR spectrometer.

2.3. Adsorption experiments

Removal of methyl orange over nano-MgO samples was carried out at room temperature (295 K). In a typical

system, 0.10 g MgO bulks was added into 200 mL methyl orange solution (40 mg L^{-1}) and intensively stirred. At regular time intervals, 5 mL solution was sampled and centrifuged for 5 min, and the supernatant solution of methyl orange was analyzed by a UV–vis spectrophotometer (Jasco V-550, Japan). The equilibrium adsorption capacities (q_e) and removal efficiency (E) are defined as follows:

$$q_e\left(mgg^{-1}\right)=\left(C_o-C_e\right)\times V/M \tag{1}$$

$$E(\%)=\left(C_o-C_e\right)/C_o\times 100\% \tag{2}$$

where C_o (mg L^{-1}) and C_e (mg L^{-1}) are the initial and equilibrium concentrations of methyl orange dye in solution, respectively. V (L) is the volume of dye solution, and M (g) is the mass of MgO adsorbent. q_e (mg g^{-1}) is the adsorption amount of methyl orange per unit mass of MgO sample.

2.4. Adsorption isotherms

The adsorption isotherm models such as Langmuir, Temkin, and Freundlich models were performed for evaluation of the distribution of methyl orange between aqueous solution and MgO bulks at an equilibrium state. The equation of Langmuir isotherm can be given as:

$$C_e/q_e=C_e/q_{\max}+1/\left(K_L\cdot q_{\max}\right)i \tag{3}$$

where q_{max} (mg g^{-1}) is the maximum adsorption concentration of methyl orange per unit mass of MgO adsorbed by the monolayer converge. K_L (L mg^{-1}) is the Langmuir adsorption constant.

The equation of Temkin isotherm mode is defined as:

$$q_e=\beta\, In\alpha+\beta\, In\, C_e \tag{4}$$

where

$$\beta=RT/b \tag{5}$$

The β and α are the Temkin constants. T (K) is the absolute temperature of system. R (8.314 J mol^{-1} K) is the universal gas constant, and b (J mg^{-1}) is the Temkin constant of adsorption heat.

The linearized form of Freundlich equation is expressed as:

$$Inq_e=InK_F+1/nInC_e \tag{6}$$

where K_F (L mg^{-1}) is the Freundlich adsorption constant, and $1/n$ is the adsorption intensity constant of adsorbent system.

2.5. Adsorption model

The pseudo-first and pseudo-second order models were employed to predict the removal kinetics of methyl orange over synthesized MgO with different nanostructures. The pseudo-first order model [32,33] can be obtained as:

$$In\left(q_e-q_t\right)=Inq_e-k_f t \tag{7}$$

where k_f (min^{-1}) is the pseudo-first order rate constant.

The pseudo-second order model [29,30,32,34] can be expressed as:

$$t/q_t=1/k_s q_e^2+t/q_e \tag{8}$$

where k_s (min^{-1}) is the pseudo-first order rate constant.

Intra-particle diffusion model [25,32,33] was employed to describe the adsorption behavior of methyl orange dye on nano-MgO bulks, which can be described as:

$$q_t=k_{dif}t^{0.5}+C \tag{9}$$

where k_{dif} (mg g^{-1} $min^{1/2}$) is the intra-particle diffusion rate constant, and C is the film thickness.

3. Results and discussion

3.1. Characterization of MgO

Fig. 2 presents the XRD patterns of MgO_L, MgO_F, and MgO_R nanoparticles prepared by different route. The typical peaks at diffraction angles of 37.0°, 43.0°, 62.4°, 74.8°, and 78.7° are all assigned to MgO phases (JCPDS, 65-0476), which can be indexed to the lattice planes of (111), (200), (220), (311), and (222), respectively [14,15]. The peaks intensity of MgO_L sample generated at 1023 K are higher than those of MgO_F calcined at 923 K. The peaks of MgO_R sample prepared at 1173 K are broader and lower than MgO_F and MgO_L. It's ascribed to the variation of MgO precursors and the different calcination temperature. The precursor of MgO_L as well as MgO_F is $Mg_5(CO_3)_4(OH)_2{\cdot}4H_2O$ prepared by paraffin/water interface precipitation, and the precursor of MgO is $5Mg(OH)_2{\cdot}MgSO_4{\cdot}3H_2O$ generated by hydrothermal route.

TEM and SEM images were performed the nanostructure of as-obtained MgO_F samples. MgO sample is flower-like hierarchical structure (Figs. 3A and B), of which the

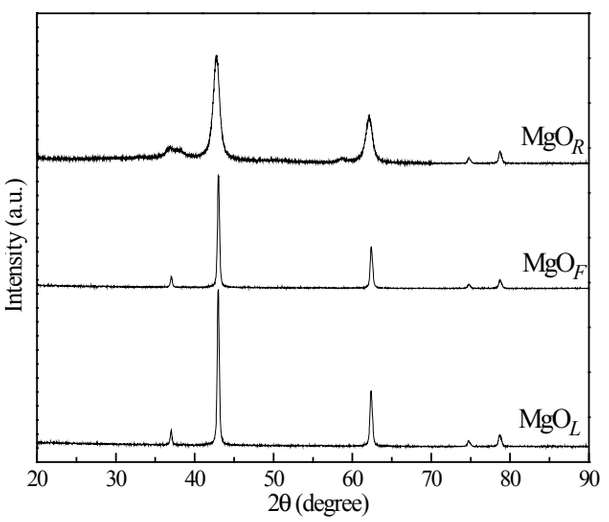

Fig. 2. XRD patterns of different MgO samples.

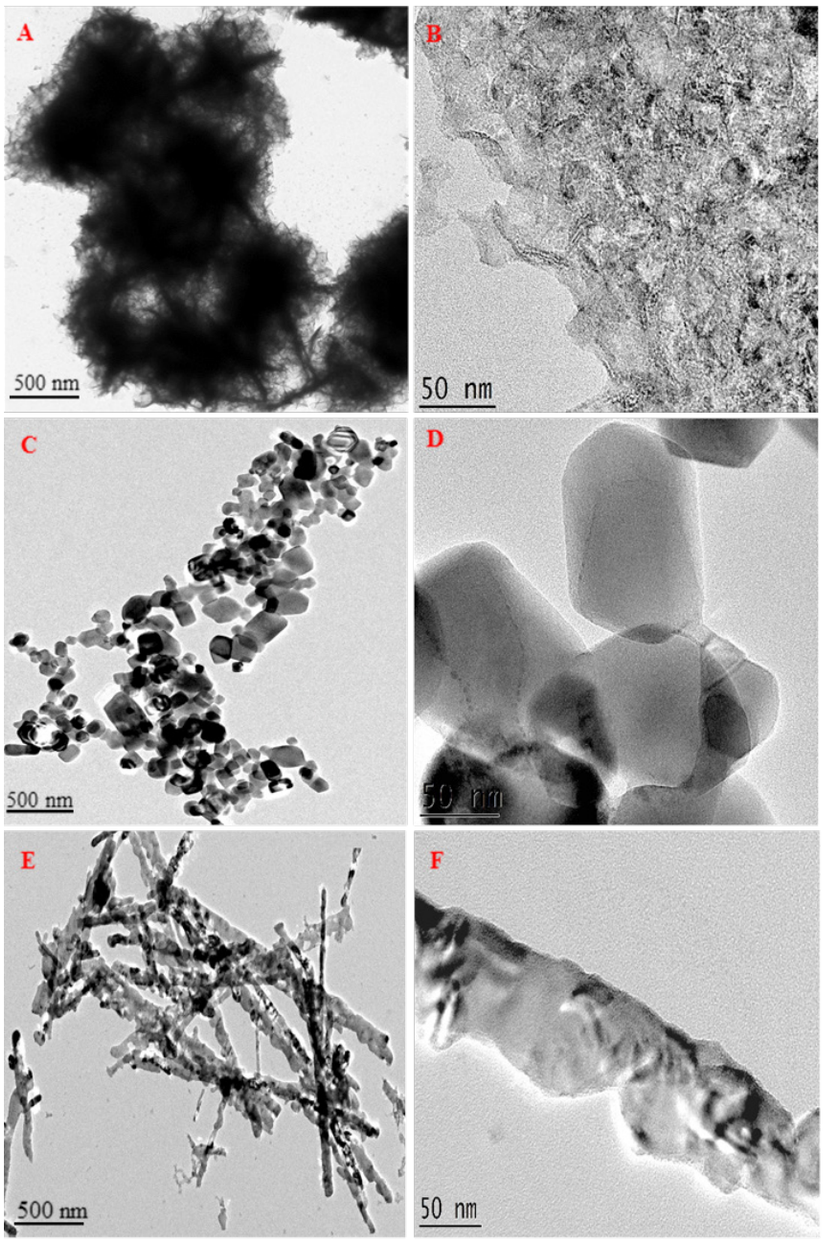

Fig. 3. TEM images of MgO samples prepared by different methods.

particle size and lamellar thickness of MgO_F are 3 μm and 30 nm, respectively (Fig. 4A and B). With the increasing temperature from 873 K to 1123 K, the small MgO crystallite blocks departs from MgO nanosheets (Figs. 4C and D) and further generates lamellar MgO with the particle size of around 60 nm (Figs. 3C and D), leading to the collapse of flower-like structured MgO sample. MgO rods generated from $5Mg(OH)_2{\cdot}MgSO_4{\cdot}3H_2O$ precursor exhibits the length of 2~4 μm and the average diameter of 50 nm, as shown in Figs. 3E and F.

N_2 adsorption-desorption isotherms of MgO_F, MgO_L, and MgO_R samples can be classified as type IV according to the IUPAC classification (Fig. 5A), confirming the formation of non-uniform slit-sharped pores in MgO samples. The pore size distribution (Fig. 5B) suggests that these MgO samples exhibit the mesopores and/or macropores structures with irregular pores. In contrast with MgO_F and MgO_L samples, MgO_R presents bigger irregular pores and larger specific surface area (Table 1), which play important role in adsorption of organic dyes from the effluents.

As presented in Fig. 6, the broad bands of as-synthesized and used MgO samples in the FT-IR spectrum ranged from 3600 to 3200 cm^{-1} are ascribed

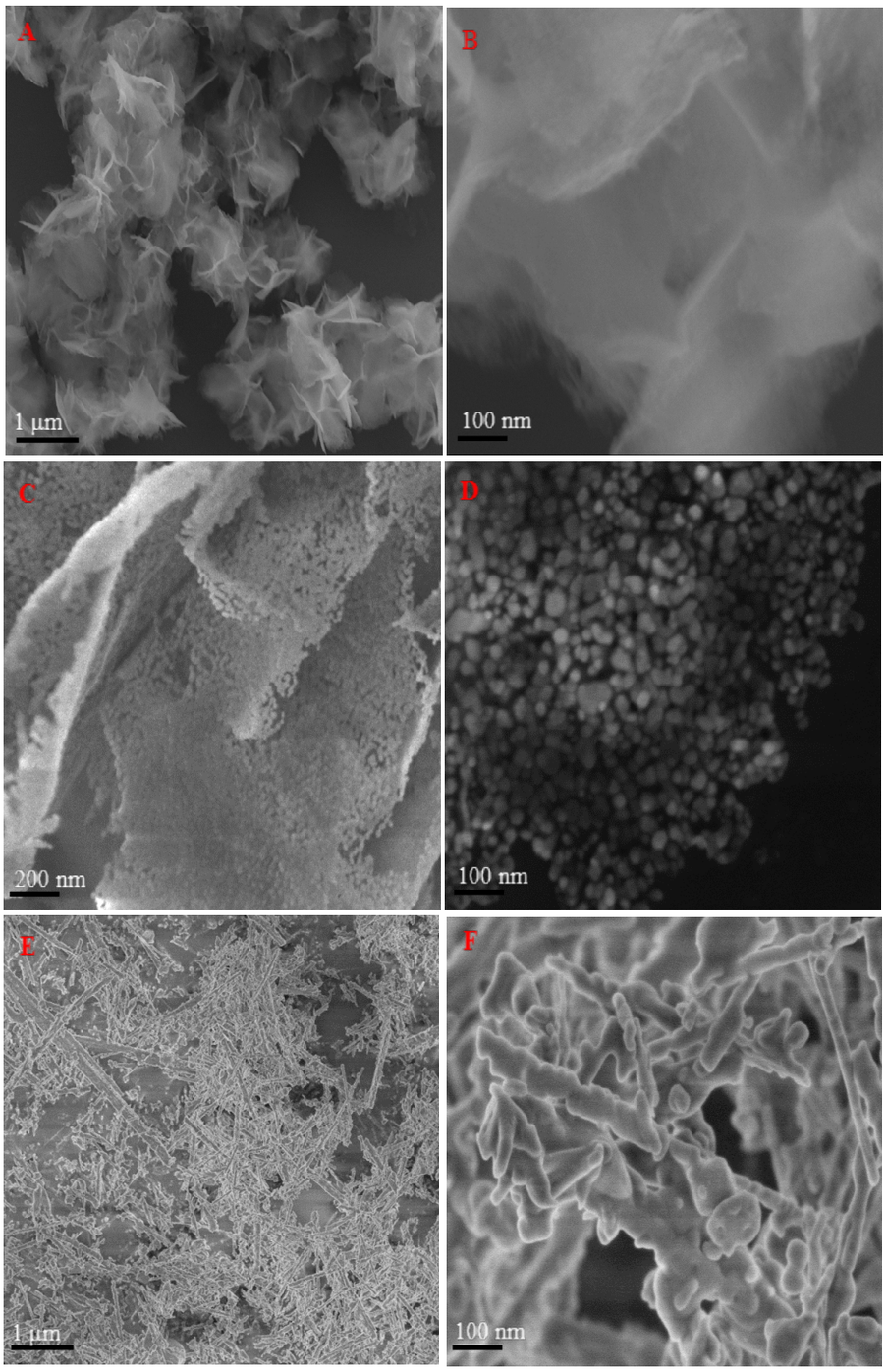

Fig. 4. SEM images of MgO (A and B), MgO (C and D), MgO (E and F).

to the asymmetric and symmetric stretching modes of hydroxyl group (ν_{as}(O-H) and ν_s(O-H)), meaning the water molecules adsorbed on the MgO surface [30,35]. In addition, the bending modes of adsorbed water molecules (δ(H-O-H)) appear at a weak peak around 1636 cm^{-1} [25,28,33]. As shown in Fig. 6B, the sharp peak at near 3700 cm^{-1} for used MgO bulks is ascribed to the free hydroxyl group (–OH) resulting from the absorption of residual H_2O. The bands extending from 1500 to 1400 cm^{-1} are assigned to the Mg-O-Mg deformation vibrations and MgO stretching vibrations, and the bands near 1100 cm^{-1} are Mg-OH vibrations [32,33]. Due to the differences in the calcination temperature of MgO precursors, the stretching vibrations of MgO_R, MgO_F, and MgO_L

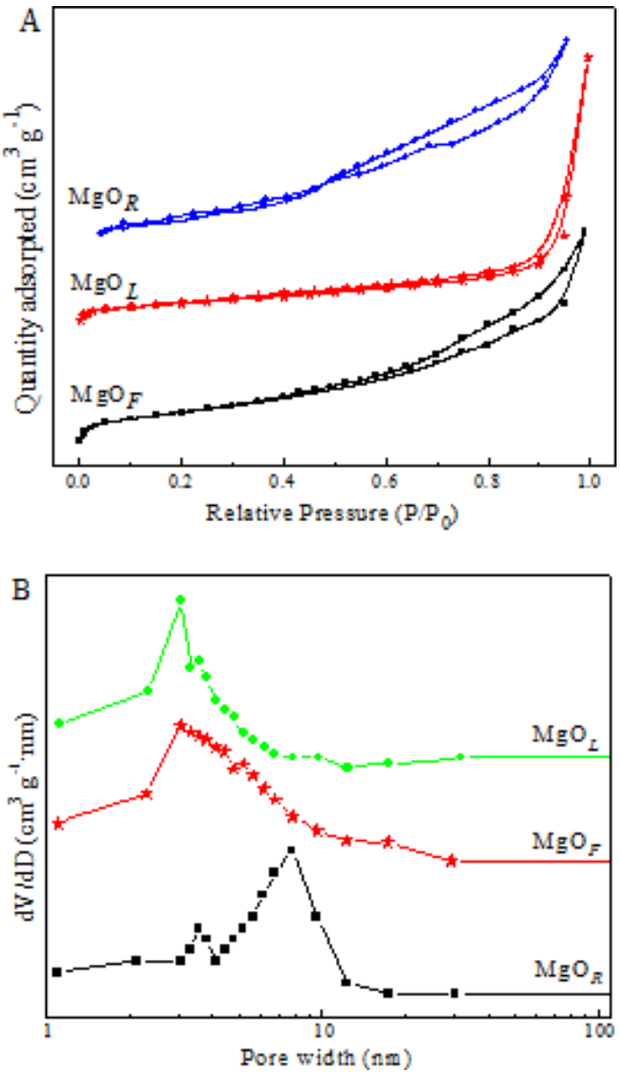

Fig. 5. N_2 sorption isotherms and pore size distributions of MgO samples.

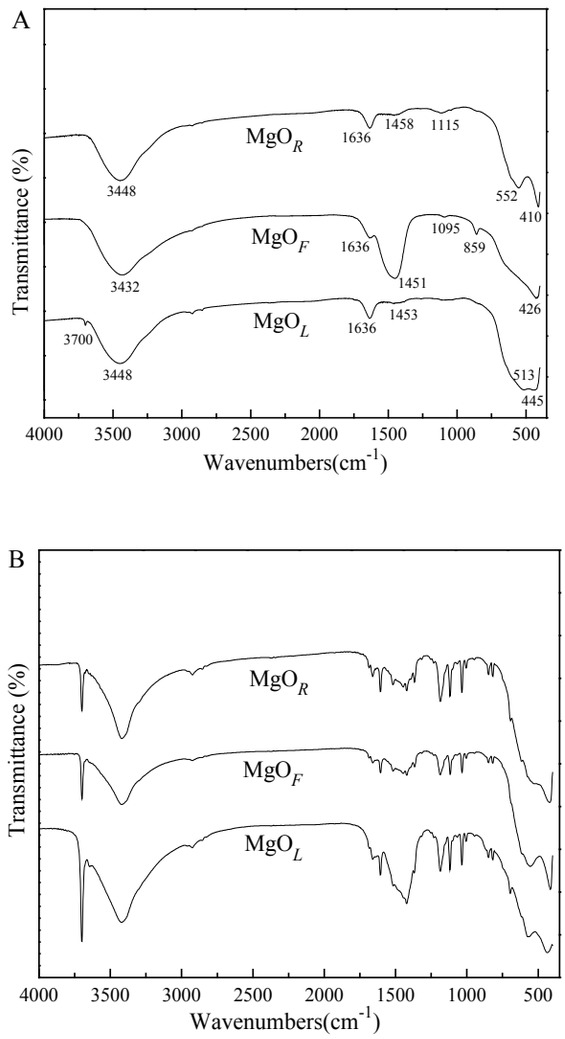

Fig. 6. FT-IR spectra of MgO samples before and after removal of methyl orange.

Table 1
Surface parameters of MgO samples

Samples	BET surface area($m^2 g^{-1}$)	Pore volume ($cm^3 g^{-1}$)	Pore diameter (nm)
MgO_F	247.36	0.30	3.43
MgO_L	130.88	0.22	3.08
MgO_R	321.08	0.37	3.85

samples are located at around 552, 859, and 513 cm^{-1}, and the bending modes of these MgO samples appear at 410, 426, and 445 cm^{-1}, respectively. As shown in Fig. 6B, several new peaks of are detected in the FI-IR spectrum of used MgO samples due to the typical vibration modes of organic group. For example, the peak at near 1640 cm^{-1} for used MgO adsorbents can be assigned to the C=O stretching vibrations [35,38,39].

3.2. *Adsorption experiments*

The adsorption capacity of MgO is greatly affected by the MgO dosage,dye concentration, pH value, and contact time [10,15,20,35]. MgO dosage is crucial to the available adsorption sites and contact areas between dye molecules and MgO. The increase in adsorbent dosage is responsible for the increasing removal efficiency. Excess of MgO is not likely to adsorb organic dye at the saturated equilibrium state of adsorption process [38,40]. Due to the high contact frequency between dye molecules and MgO active sites, equilibrium time of adsorption decreases with the increasing methyl orange concentration. The pH value is a critical factor of the charge transfer of liquid/solid interface in adsorption system [26,27]. High pH value leads to the less proto nation of functional groups of organic dye, and low pH value (high H^+) induces to the transfer of MgO solid into Mg^{2+} ions, leading to the inferior removal efficiency of

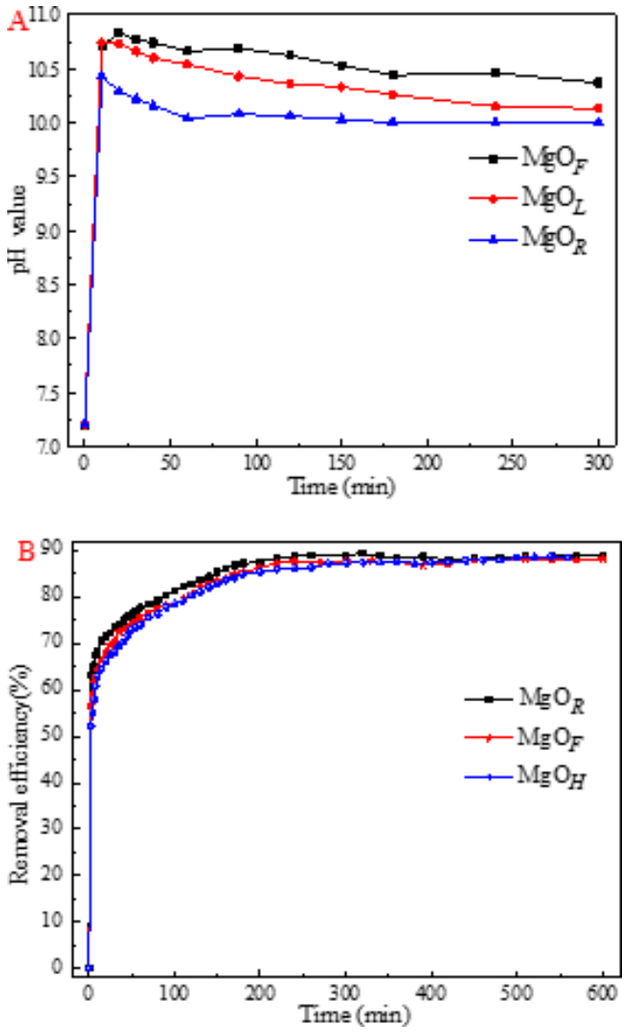

Fig. 7. Effect of contact time on pH value of solution (A) and removal efficiency of methyl orange (B) on different MgO samples.

methyl orange. As shown in Fig. 7A, pH value of methyl orange solution (40 mg L^{-1}) is 7.20, and the initial pH values of solution with presence of MgO_F, MgO_L, and MgO_R bulks are 10.82, 10.50, and 10.22, respectively. The pH values of these adsorption systems slightly decreased with the increasing contact time due to the reduction of MgO active sites, of which MgO_R was higher than those of MgO_F and MgO_L samples.

As shown in Fig. 7B, the adsorption capacity of MgO samples for the removal of methyl orange increased rapidly within 200 min due to the availability of adsorption sites. The removal efficiency enhanced slowly with the increasing contact time. The vacant surface sites are occupied and reached saturating adsorption after a certain time, leading to the repulsive force created by methyl orange molecules on the MgO surface and solution phase. Compared with MgO_F and MgO_L, MgO_R exhibited shorter equilibrium time of adsorption and higher removal efficiency for methyl orange. It could be ascribed to the large surface area and the sufficient active sites of MgO sample.

3.3. Adsorption isotherms

Adsorption isotherms are widely employed to describe the dynamic equilibrium relationship between adsorbent and adsorbate. Langmuir, Temkin, and Freundlich adsorption isotherm experiments were investigated by adding 20 mg MgO bulks with different nanostructures to 40 mL methyl orange solution with a concentration ranged from 20 mg L^{-1} to 100 mg L^{-1} at 298 K. The correlation efficient (R^2) of Langmuir isotherm (Table 2 and Fig. 8) is higher than that of Temkin isotherm and Freundlich isotherm, indicating that Langmuir isotherm can well describe the adsorption process of methyl orange on different MgO samples. The removal of methyl orange on MgO bulks with different microstructure is involved in the monolayer coverage at specific active sites on MgO surface, which is agreed with previous works [3,4,8,19, 31,39]. The heterogeneous adsorbents such as EDTA functionalized magnetic graphene oxide [46], magnetic Fe_3O_4/MgAl-LDH composite [47] and NH_2-rich polymer/graphene oxide [48] are the multi molecular layers of coverage due to the heterogeneous active sites. The constant K_R of Langmuir isotherm model of MgO_R (Table 2) is larger than that of MgO_F and MgO_L samples due to its high surface area and large pore volume. The maximum adsorption quantity of methyl orange on MgO_R, MgO_F and MgO_L samples based on the Langmuir model are 131.1, 123.7 and 107.3 mg g^{-1}, respectively. It can be concluded that the adsorption capacity of MgO samples with different nanostructure are greatly affected by the synthesis routes.

3.4. Adsorption model

Pseudo-first-order, pseudo-second-order, and intra-particle diffusion models were performed for the investigation of removal kinetics of different MgO samples, as shown in Fig. 9. The correlation coefficients (R^2) of pseudo-first-order (Table 3) are lower than those of pseudo-second-order adsorption models, and q_e values of pseudo-second-order adsorption model fit well with the experimental results, confirming the validity of the pseudo-second-order adsorption model for the removal of methyl orange on MgO samples. The rate constant value for pseudo-second-order reaction model of MgO_R adsorbent is higher than that of MgO_F and MgO_L samples. It can be attributed to the available accessibility to active sites for bulk adsorption of methyl orange.

The adsorption system of MgO for the removal of methyl orange is surface diffusion coupled with pore diffusion, as plotted in Fig. 9. Initial intra-particle transport is the rapid occupation of specific active sites on MgO surface, and the following step is the diffusion of organic dye molecules from the surface sites into the inner pores. The linear plots of intra-particle diffusion model for the removal of methyl orange on different MgO samples do not get through the origin (Fig. 9). It's concluded that the rate-determining step of adsorption process is the boundary layer/film diffusion [32]. The diffusion rate constant $k_{dif1}$of MgO_R adsorbent (Table 4) is higher than that of MgO_F and MgO_L, indicat-

Table 2
Isotherm parameters for the removal of methyl orange on different MgO samples

Samples	Langmuir isotherm model			Temkin isotherm model				Freundlich isotherm model		
	q_{max}(mg g^{-1})	K_L(L min^{-1})	R^2	α	β	b (J mg^{-1})	R^2	K_F(Lmg^{-1})	n	R^2
MgO_F	123.7	6.28	0.997	1.18	27.6	91.3	0.993	26.2	2.28	0.978
MgO_L	107.3	5.98	0.996	1.41	28.3	89.0	0.995	23.6	2.26	0.981
MgO_R	131.1	6.64	0.998	1.51	30.1	83.8	0.994	27.7	2.18	0.985

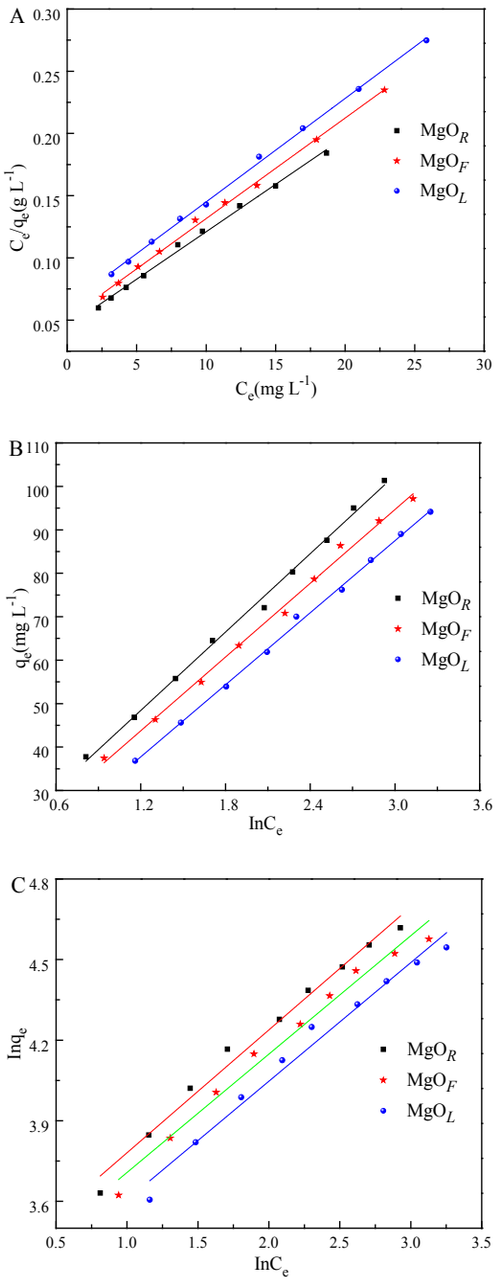

Fig. 8. Langmuir isotherms (A), Temkin isotherms (B), and Freundlich isotherms (C) for removal of methyl orange on different MgO samples.

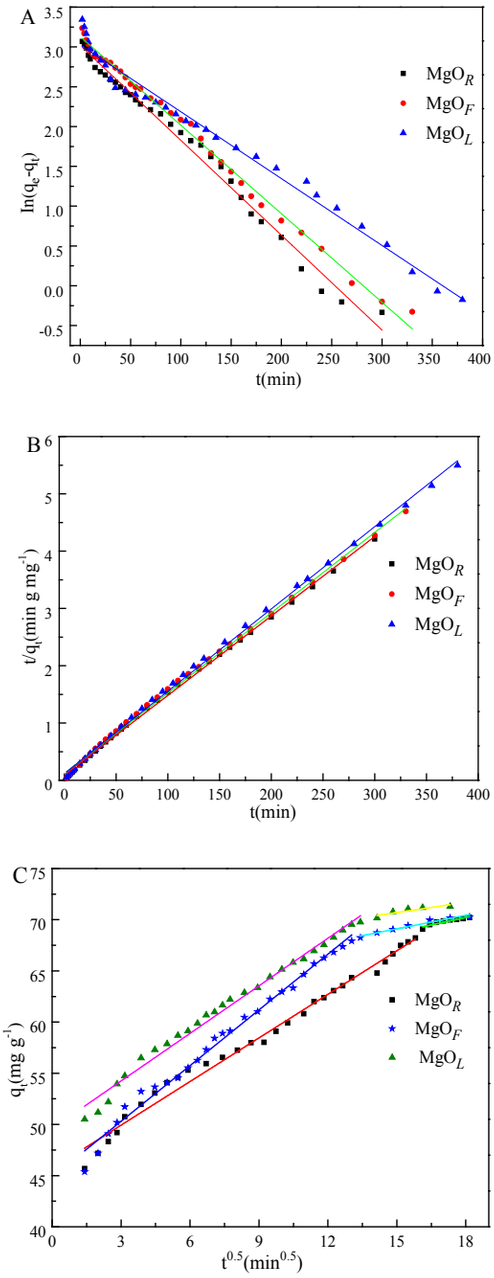

Fig. 9. Pseudo first-order kinetics (A), second-order kinetics (B), and intra-particle diffusion kinetics (C) for removal of methyl orange on different MgO samples.

Table 3
Kinetic parameters for the removal of methyl orange on MgO samples

Samples	Pseudo-first-order			Pseudo-second-order		
	$q_{e,cal}$ (mg g^{-1})	K_L (L min^{-1})	R^2	$q_{e,cal}$ (mg g^{-1})	k_1 (mg g^{-1} min^{-1})	R^2
MgO_F	21.0	0.011	0.989	69.6	0.0018	0.999
MgO_L	20.7	0.008	0.995	68.3	0.0016	0.998
MgO_R	22.9	0.012	0.982	72.1	0.0021	0.998

Table 4
Kinetic parameters of the intra-particle diffusion of different MgO samples for the removal of methyl orange

Samples	k_{difl} (mg g^{-1} min$^{-1/2}$)	C_1	R_1^2	k_{difl} (mg g^{-1} min$^{-1/2}$)	C_2	R_2^2
MgO_F	1.49	49.5	0.987	0.330	64.5	0.832
MgO_L	1.42	45.7	0.986	0.489	61.4	0.858
MgO_R	1.81	44.8	0.988	0.442	62.4	0.954

ing that MgO is an excellent candidate for the removal of methyl orange.

4. Conclusion

MgO_R synthesized by a hydrothermal method exhibited better adsorption capacity than those of MgO_F and MgO_L nanomaterials generated by a micro emulsion route. It's attributed to the higher specific surface area, larger pore volume, and more available active sites of MgO_R. Langmuir isotherm model and pseudo-second-order model were suitable to describe the adsorption isotherm and adsorption kinetics of MgO for the removal of methyl orange, respectively. The adsorption process of MgO was the combination of immediate surface diffusion and slow pore diffusion, of which the rate-determining step was the boundary layer/film diffusion. MgO adsorbent with excellent physical properties is a promising adsorbent for the removal organic dyes.

Acknowledgements

The authors gratefully acknowledge the financial support of this work by National Natural Science Foundation of China (Grant NO: 21506103 and 51608512), Science and Technology Support Program of Sichuan Province (Grant NO: 2015GZ0170), Major Training Program of the Education Department of Sichuan Province (Grant NO: 15CZ0026 and and 17CZ0019), and The science and technology research project of Chongqing municipal education commission of China (KJ1601334).

References

[1] M.A. Rauf, S.S. Ashraf, Survey of recent trends in biochemically assisted degradation of dyes: a review, Chem. Eng. J., 209 (2012) 520–530.
[2] N. Rakmak, W. Wiyaratn, C. Bunyakan, J. Chungsiriporn, Synthesis of Fe/MgO nano-crystal catalysts by sol–gel method for hydrogen sulfide removal, Chem. Eng. J., 162 (2010) 84–90.
[3] A.T. Vu, S. Jiang, K. Ho, J.B. Lee, C.H. Lee, Mesoporous magnesium oxide and its composites: preparation, characterization, and removal of 2-chloroethyl ethyl sulfide, Chem. Eng. J., 269 (2015) 82–93.
[4] C. Cao, J. Qu, F. Wei, H. Liu, W. Song, Superb adsorption capacity and mechanism off lower like magnesium oxide nanostructures for lead and cadmium ions, ACS Appl. Mater. Inter., 4 (2012) 4283–4287.
[5] V. Srivastava, Y.C. Sharma, M. Sillanpää, Green synthesis of magnesium oxide nano flower and its application for the removal of divalent metallic species from synthetic wastewater, Ceram. Int., 41 (2015) 6702–6709.
[6] F. Ciesielczyk, P. Bartczak, T. Jesionowski, Removal of nickel(II) and cadmium(II) ions from aqueous solutions using an oxide adsorbent of MgO center dot SiO_2 type, Desal. Water Treat., 55 (2015) 1271–1284.
[7] C. Xiong, W. Wang, F. Tan, F. Luo, J. Chen, X. Qiao, Investigation on the efficiency and mechanism of Cd(II) and Pb(II) removal from aqueous solutions using MgO nanoparticles, J. Hazard. Mater., 299 (2015) 664–674.
[8] B. El-Gammal, M.A. Hamid, G.M. Ibrahim, Ion-exchange properties of ternary CaO-MgO-Al_2O_3 spinels in pH-controlled aqueous radioactive waste solutions, Desal. Water Treat., 53 (2015) 2464–2480.
[9] Q.A. Wang, J.Z. Luo, Z.Y. Zhong, A. Borgna, CO_2 capture by solid adsorbents and their applications: current status and new trends, Energy Environ. Sci., 4 (2011) 42–55.
[10] P. Tian, X. Han, G. Ning, H. Fang, J. Ye, W. Gong, Y. Lin, Synthesis of poroushier archical MgO and its superb adsorption properties, ACS Appl. Mater. Inter., 5 (2013) 12411–12418.
[11] C. Pighini, T. Belin, J. Mijoin, P. Magnoux, G. Costentin, H. Lauron-Pernot, Micro calorimetric and thermodynamic studies of CO_2 and methanol adsorption on magnesium oxide, Appl. Surf. Sci., 257 (2011) 6952–6962.
[12] D.L. Meixner, D.A. Arthur, S.M. George, Kinetics of desorption, adsorption, and surface diffusion of CO_2 on MgO (100), Surf. Sci., 261 (1992) 141–154.
[13] Y. Haldorai, J.J. Shim, An efficient removal of methyl orange dye from aqueous solution by adsorption onto chitosan/MgO composite: A novel reusable adsorbent, Appl. Surf. Sci., 292 (2014) 447–453.
[14] W.J. Liu, H. Jiang, K. Tian, Y.W. Ding, H.Q. Yu, Mesoporous carbon stabilized MgO nanoparticles synthesized by pyrolysis of $MgCl_2$ preloaded waste biomass for highly efficient CO_2 capture, Environ. Sci. Technol., 47 (2013) 9397–9403.
[15] G. Guo, Adsorption characteristics and mechanisms of high-levels of ammonium from swine wastewater using natural and MgO modified zeolites, Desal. Water Treat., 57 (2016) 5452–5463.
[16] Y. Rao, W. Wang, F. Tan, Y. Cai, J. Lu, X. Qiao, Influence of different ions doping on the antibacterial properties of MgO nanopowders, Appl. Surf. Sci., 284 (2013)726–731.
[17] Z. Zhou, Q. Sun, Z. Hu, Y. Deng, Nano belt formation of magnesium hydroxide sulfate hydrate via a soft chemistry process, J. Phys. Chem., B 110 (2006) 13387–13392.

[18] S. Dadvar, H. Tavanai, M. Morshed, M. Ghiaci, The removal of 2-chloroethylethyl sulfide using activated carbon nanofibers embedded with MgO and Al_2O_3 nanoparticles, J. Chem. Eng., Data, 57 (2012) 1456–1462.
[19] X. Wu, H. Cao, G. Yin, J. Yin, Y. Lu, B. Li, $MgCO_3 \cdot 3H_2O$ and MgO complex nanostructures: controllable biomi metic fabrication and physical chemical properties, Phys. Chem. Chem. Phys., 13 (2011) 5047–5052.
[20] H.R. Mahmoud, S.A. El-Molla, M. Saif, Improvement of physico chemical properties of Fe_2O_3/MgO nanomaterials by hydrothermal treatment for dye removal from industrial wastewater, Powder Technol., 249 (2013) 225–233.
[21] Z. Wei, H. Qi, P. Ma, J. Bao, A new route to prepare magnesium oxide whisker, In org. Chem. Commun., 5 (2002) 147–149.
[22] Y.H. Kim, V.A. Tuan, M.K. Park, C.H. Lee, Sulfur removal from municipal gas using magnesium oxides and a magnesium oxide/silicon dioxide composite, Micropor. Mesopor. Mater., 197 (2014) 299–307.
[23] A.T. Vu, Y. Park, P.R. Jeon, C.-H. Lee, Mesoporous MgO sorbent promoted with KNO_3 for CO_2 capture at intermediate temperatures, Chem. Eng. J., 258 (2014) 254–264.
[24] A.T. Vu, K. Ho, S. Jin, C.H. Lee, Double sodium salt-promoted mesoporous MgO sorbent with high CO_2 sorption capacity at intermediate temperatures under dry and wet conditions, Chem. Eng. J., 291 (2016) 161–173.
[25] G. Song, X. Zhu, R. Chen, Q. Liao, Y.D. Ding, L. Chen, An investigation of CO_2 adsorption kinetics on porous magnesium oxide, Chem. Eng. J., 283 (2016) 175–183.
[26] D.A. Yang, H.Y. Cho, J. Kim, S.T. Yang, W.S. Ahn, CO_2 capture and conversion using Mg-MOF-74 prepared by a sono chemical method, Energy Environ. Sci., 5(2012) 6465–6473.
[27] K.K. Han, Y. Zhou, Y. Chun, J.H. Zhu, Efficient MgO-based mesoporous CO_2 trapper and its performance at high temperature, J. Hazard. Mater., 203–204 (2012) 341–347.
[28] G. Qi, L. Fu, B.H. Choi, E.P. Giannelis, Efficient CO_2 sorbents based on silica foam with ultra-large mesopores, Energy Environ. Sci., 5 (2012) 7368–7375.
[29] M. Toor, B. Jin, Adsorption characteristics, isotherm, kinetics, and diffusion of modified natural bentonite for removing diazo dye, Chem. Eng. J., 187 (2012) 79–88.
[30] T.G. Venkatesha, R. Viswanatha, Y.A. Nayaka, B.K. Chethana, Kinetics and thermo dynamics of reactive and vat dyes adsorption on MgO nanoparticles, Chem. Eng. J., 198–199 (2012) 1–10.
[31] C. Gao, W. Zhang, H. Li, L. Lang, Z. Xu, Controllable fabrication of mesoporous MgO with various morphologies and their absorption performance for toxic pollutants in water, Cryst. Growth Des., 8 (2008) 3785–3790.
[32] H.R. Mahmoud, S.M. Ibrahim, S.A. El-Molla, Textile dye removal from aqueous solutions using cheap MgO nanomaterials: Adsorption kinetics, isotherm studies and thermodynamics, Adv. Powder Technol., 27(1) (2016) 223–231.
[33] M. Toor, B. Jin, Adsorption characteristics, isotherm, kinetics, and diffusion of modified natural bentonite for removing diazo dye, Chem. Eng. J., 187 (2012) 79–88.
[34] M.S. Mastuli, N. Kamarulzaman, M.A. Nawawi 1, A.M. Mahat, R. Rusdi, N. Kamarudin, Growth mechanisms of MgO nanocrystals via a sol–gel synthesis using different complexing agents, Nanoscale Res. Lett., 134 (2014) 1–9.
[35] J. Feng, L. Zou, Y. Wang, B. Li, X. He, Z. Fan, Y. Ren, Y. Lv, M. Zhang, D. Chen, Synthesis of high surface area, mesoporous MgO nanosheets with excellent adsorption capability for Ni(II) via a distillation treating, J. Colloid Interf. Sci., 438 (2015) 259–267.
[36] X.Y. Yu, T. Luo, Y. Jia, Y.X. Zhang, J.H. Liu, X.J. Huang, Porous hierarchically micro-/nanostructured MgO: Morphology control and their excellent performance in As(III) and As(V) removal, J. Phys. Chem. C., 115 (2011) 22242–22250.
[37] M. Hua, S. Zhang, B. Pan, W. Zhang, L. Lv, Q. Zhang, Heavy metal removal from water/wastewater by nano sized metal oxides: A review, J. Hazard. Mater., 211 (2012) 317–331.
[38] S. Li, B. Zhou, B. Ren, L. Xing, L. Tan, L. Dong, J. Li, Preparation of MgO nanomaterials by micro emulsion-based oil/water interface precipitation, Mater. Lett., 171 (2016) 204–207.
[39] P. Tian, X. Han, G. Ning, H. Fang, J. Ye, W. Gong, Y. Lin, Synthesis of poroushier archical MgO and its superb adsorption properties, ACS Appl. Mater. Inter., 5 (2013) 12411–12418.
[40] L. Zhang, W. Zhu, H. Zhang, S. Bi, Q. Zhang, Hydrothermal–thermal conversion synthesis of hierarchical porous MgO microrods as efficient adsorbents for lead (II) and chromium (VI) removal, RSC Adv., 58 (2014) 30542–30550.
[41] M. Kermani, F.B. Asl, M. Farzadkia, A. Esrafili, S.S. Arian, M. Khazaei, Y.D. Shahamat, D. Zeynalzadeh, Heterogeneous catalytic ozonation by Nano-MgO is better than sole ozonation for metronidazole degradation, toxicity reduction, and biodegradability improvement, Desal. Water Treat., 57 (2016) 16435–16444.
[42] H. Yan, X.H. Zhang, J.M. Wu, L.Q. Wei, X.G. Liu, B.S. Xu, The use of CTAB to improve the crystallinity and dispersibility of ultrafine magnesium hydroxide by hydrothermal route, Powder Technol., 188 (2008) 128–132.
[43] M. Nazari, R. Halladj, Optimization of fluoride adsorption onto a sonochemically synthesized nano-MgO/γ-Al_2O_3 composite adsorbent through applying the L16 Taguchi orthogonal design, Desal. Water Treat., 56 (2015) 2464–2476.
[44] X. Sun, L. Xiang, Hydrothermal conversion of magnesium oxysulfate whiskers to magnesium hydroxide nanobelts, Mater. Chem. Phys., 109 (2008) 381–385.
[45] K.H. Kang, D.K. Lee, Synthesis of magnesium oxysulfate whiskers using triethanolamine as a morphology control agent, J. Ind. Eng. Chem., 20 (2014) 2580–2583.
[46] L. Cui, Y. Wang, L. Gao, L. Hu, L. Yan, Q. Wei, B. Du, EDTA functionalized magnetic graphene oxide for removal of Pb(II), Hg(II) and Cu(II) in water treatment: Adsorption mechanism and separation property, Chem. Eng. J., 281 (2015) 1–10.
[47] R.R. Shan, L.G. Yan, K. Yang, S.J. Yu, Y.F. Hao, H.Q. Yu, B. Du, Magnetic Fe_3O_4/Mg Al-LDH composite for effective removal of three red dyes from aqueous solution, Chem. Eng. J., 252 (2014) 38–46.
[48] H.T. Xing, J.H. Chen, X. Sun, Y.H. Huang, Z.B. Su, S.R. Hu, W. Weng, S.X. Li, H.X. Guo, W.B. Wu, NH_2-rich polymer/graphene oxide use as a novel adsorbent for removal of Cu(II) from aqueous solution, Chem. Eng. J., 263 (2015) 280–289.